ACS NANO

www.acsnano.org

Wafer-Scale Transfer and Integration of Tungsten-Doped Vanadium Dioxide Films

Yuan Li, He Ma,* Run Shi, Yonghuang Wu, Shifeng Feng, Yulan Fu, Yuanqi Wei, Xuzhe Zhao, Kaichen Dong, Kaili Jiang, Kai Liu,* and Xinping Zhang*

Cite This: *ACS Nano* 2025, 19, 6209−6220

Read Online

ABSTRACT: Modern optoelectronic devices trend toward greater flexibility, wearability, and multifunctionality, demanding higher standards for fabrication and operation temperatures. Vanadium dioxide (VO_2), with its metal−insulator transition (MIT) at 68 °C, serves as a crucial functional layer in many optoelectronic devices. However, VO_2 usually needs to grow at >450 °C in an oxygen-containing atmosphere and to function across its MIT temperature, leading to low compatibility with most optoelectronic devices, especially on flexible substrates. In this work, we report a layer-by-layer transfer method of wafer-scale tungsten-doped VO_2 films, which enables sequential integration of the VO_2 films with low MIT temperatures (down to 40 °C) onto arbitrary substrates. Notably, by stacking multiple VO_2 films with different doped levels, a quasi-gradient-doped VO_2 architecture can be achieved, effectively broadening the MIT temperature window and reducing the hysteresis of VO_2. These integrated VO_2 films find a wide scope of applications in flexible temperature indicator strips, infrared camouflage devices, nonreciprocal ultrafast light modulators, and smart photoactuators. Our work promotes the development of more flexible and tunable optoelectronic devices integrated with VO_2.

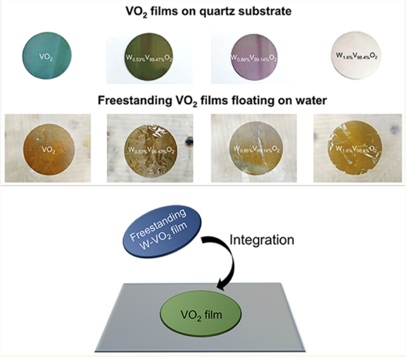

KEYWORDS: *vanadium dioxide, tungsten doping, phase transition, wafer-scale transfer, vertical integration*

1. INTRODUCTION

The development of modern electronic devices with greater flexibility, wearability, and multifunctionality demands higher standards for fabrication and operation temperatures. In electronic devices, metal oxide films are widely used as dielectric layers as well as sensing, energy harvesting, and driving layers.[1−4] As a textbook functional metal oxide, vanadium dioxide (VO_2), known for its famous metal−insulator transition (MIT) at around 68 °C, has attracted long-standing attention in the past decades.[5−10] Various methods, including magnetron sputtering,[11] pulsed laser deposition,[12] atomic layer deposition,[13] and molecular beam epitaxy,[14] have been employed to synthesize high-quality VO_2 films. For instance, stress-free VO_2 films can be grown on mica substrates, allowing for precise control over their microstructure and properties by magnetron sputtering.[15,16] Due to its MIT, VO_2 becomes an essential component in many smart devices such as self-adaptive heat management devices,[17] terahertz modulators,[18,19] microactuators,[20−22] and neurosynaptic devices.[23−25] It is crucial to develop a universal approach to integrating VO_2 films into diverse electronic devices. However, crystalline VO_2 films usually need to grow at >450 °C in an oxygen-containing atmosphere and to function across its MIT temperature,[8,26−28] leading to low compatibility with most electronic devices, especially on flexible substrates such as polyethylene terephthalate (PET, used below 150 °C), polyethylene naphthalate (PEN, used below 350 °C), thermoplastic polyurethane (TPU, used below 220 °C), and polydimethylsiloxane (PDMS, used below 350 °C).

Although the low-temperature growth of VO_2 films is achieved by several methods including structural template growth,[29,30] sol−gel synthesis,[31] and high-power impulse magnetron sputtering,[32] the relatively poor crystallinity of as-prepared VO_2 thin films is still a problem. Inspired by the transfer of van der Waals (vdW) materials, the technique for transferring freestanding oxide films to build devices has advanced rapidly in recent years because it effectively preserves the high quality of oxide films.[33−41] For VO_2, some inspiring transfer methods through sacrificial layer etching, vdW epitaxial transfer, and nanopinhole permeation-etching (NPE) have been reported.[42−46] However, current research efforts concerning freestanding VO_2 have been predominantly

Received: October 23, 2024
Revised: January 28, 2025
Accepted: January 30, 2025
Published: February 8, 2025

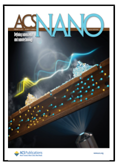

https://doi.org/10.1021/acsnano.4c15059
ACS Nano 2025, 19, 6209−6220

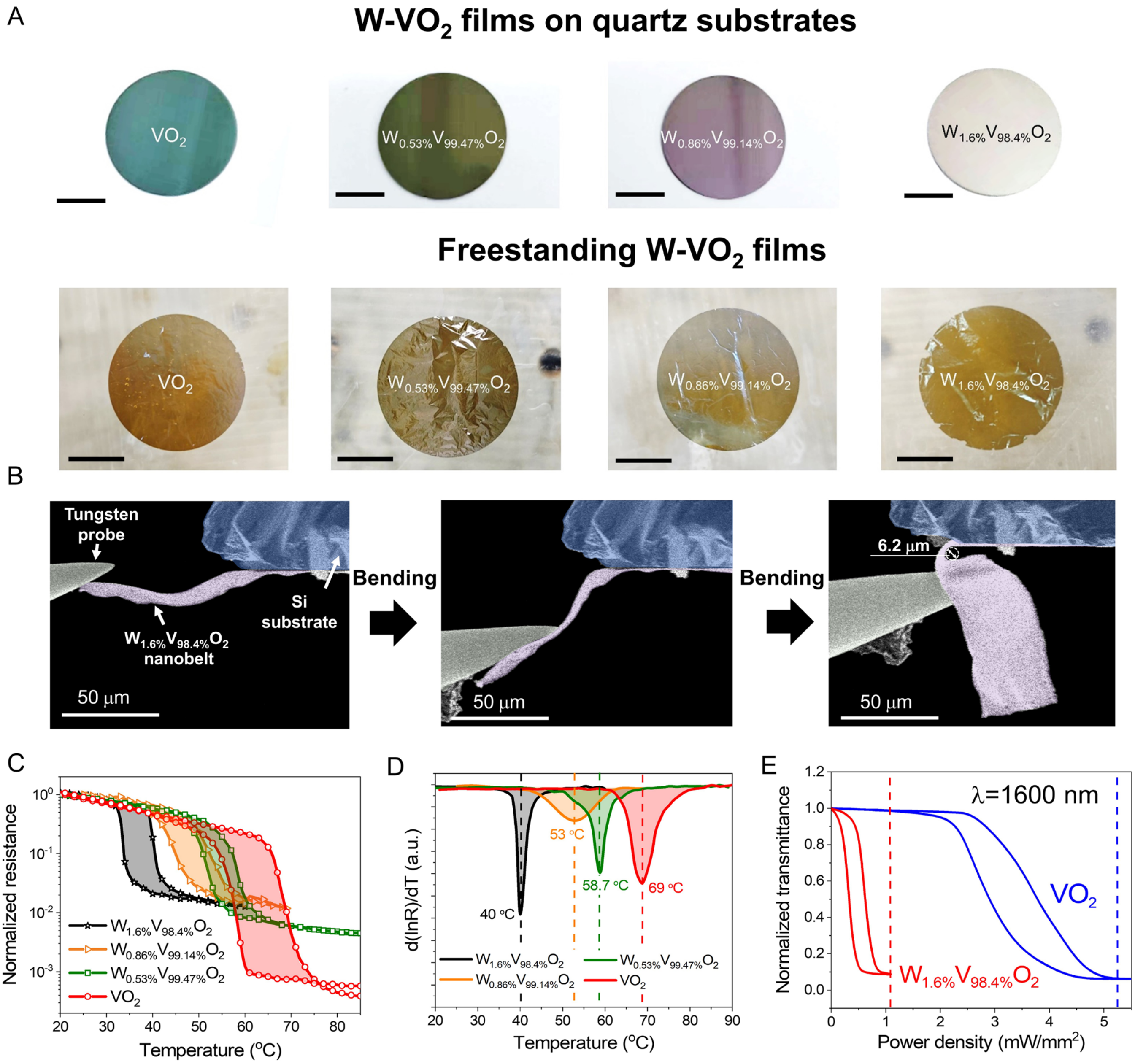

Figure 1. (A) Optical images of various films: pure VO$_2$, W$_{0.53\%}$V$_{99.47\%}$O$_2$, W$_{0.86\%}$V$_{99.14\%}$O$_2$, and W$_{1.6\%}$V$_{98.4\%}$O$_2$, all grown on a one-inch quartz substrate (upper panel), with a scale bar of 1 cm. The lower panel displays the optical images of the same set of one-inch freestanding films—VO$_2$, W$_{0.53\%}$V$_{99.47\%}$O$_2$, W$_{0.86\%}$V$_{99.14\%}$O$_2$, and W$_{1.6\%}$V$_{98.4\%}$O$_2$—floating on water, also with a scale bar of 1 cm. (B) Scanning electron microscopy (SEM) images showing the bending of a W$_{1.6\%}$V$_{98.4\%}$O$_2$ nanobelt to a curvature of 0.33 μm^{-1} using a tungsten probe. (C) Resistance–temperature (R–T) curves for various freestanding W-VO$_2$ films transferred to silicon nitride frame. (D) Derivative logarithmic plots of resistances for various freestanding W-VO$_2$ films versus temperature. (E) Transmittance changes at a wavelength of 1600 nm for freestanding W$_{1.6\%}$V$_{98.4\%}$O$_2$/carbon nanotube (CNT) film and freestanding VO$_2$/CNT film under electrical stimulation.

made for single-layer films, thereby merely delivering single-functional devices. Multiple transfer and integration of wafer-scale VO$_2$ films is essential, akin to the development of wafer-scale stacked vdW heterojunctions,[47−50] but it is still very challenging. In addition to refining the transfer technique, it is also imperative to address the issue of the relatively high MIT temperature of VO$_2$, which results in high operational temperatures and large power consumption of devices. All of these challenges must be addressed for developing large-area, multifunctional VO$_2$-integrated devices.

In this work, we report a layer-by-layer transfer of wafer-scale tungsten-doped VO$_2$ (W-VO$_2$) films, which enables sequential integration of the VO$_2$ films with low MIT temperatures (down to 40 °C) onto arbitrary substrates. The MIT temperature of the freestanding W-VO$_2$ films is well tuned by adjusting the amount of tungsten doping. By stacking multiple VO$_2$ films with different doped levels, a quasi-gradient-doped VO$_2$ architecture can be achieved, effectively broadening the MIT temperature window and reducing the hysteresis of VO$_2$. These free-standing VO$_2$ films can be integrated onto both solid and flexible substrates, as well as with other functional materials, finding a variety of applications in flexible temperature indicator strips, infrared camouflage devices, nonreciprocal ultrafast light modulators, and smart photoactuators.

2. RESULTS AND DISCUSSION

2.1. Preparation of Wafer-Scale Freestanding W-VO_2 Films. Wafer-scale W-VO_2 films with various levels of tungsten doping (Figure 1A) were deposited on SiO_2 substrates (quartz or SiO_2/Si) through reactive magnetic sputtering followed by a postannealing process, as detailed in the Experimental Section. The scanning electron microscopy (SEM) and transmission electron microscopy (TEM) images of the W-VO_2 film (Figure S1) reveal numerous nanopinholes within the film. Due to these nanopinholes, the entire W-VO_2 films could be released from the one-inch quartz substrates by using the NPE technique (Figure 1A). Specifically, the W-VO_2 film on the quartz substrate was immersed in a buffered oxide etchant (BOE, with a 5:1 volume ratio of 40% NH_4F to 49% HF) until it was almost fully separated from the substrate. As the interface between the W-VO_2 film and the substrate was etched from top to bottom, the wafer-scale W-VO_2 film could be detached from the substrate (quartz wafer with a diameter of 56 mm) within several minutes, achieving an area of ~14 cm^2 (Figure S2). The freestanding W-VO_2 film was then transferred from the BOE solution to water, enabling subsequent transfer to any arbitrary substrate (Movie S1). As demonstrated in Figure S3, the W-VO_2 film was successfully transferred to a PET substrate. The W-VO_2/PET film was easily bendable, showcasing its excellent flexibility (Movie S2). We studied the optical modulation performance on the W-VO_2/PET film both before and after subjecting it to extensive bending. During the tests, the two ends of the W-VO_2/PET film were fixed with clamps, one of which was attached to a movable stage. The film was bent by adjusting the stage until a bending strain of 5% was achieved (Figure S4A). As shown in Figure S4B, the optical modulation performance of the W-VO_2/PET film was not changed after the extensive mechanical bending. The sustainable bending strain of the W-VO_2/PET film was comparable to that reported in the literature (Table S1).

We measured the optical property of the W-VO_2/mica film after bending 10, 100, 1000, and 10,000 times (Figure S5). The modulation amplitude and MIT temperature of W-VO_2/mica at a wavelength of 1600 nm were almost constant even after bending 10,000 times, indicating the excellent mechanical stability of the freestanding W-VO_2 film. The mechanical properties of the freestanding W-VO_2 film were further examined using a micromanipulator mounted in the SEM. Freestanding W-VO_2 nanobelts were prepared through a direct-laser-writing method, as described in our previous work.[51] One end of the W-VO_2 nanobelt was anchored to the Si substrate, while the other end was bent using the micromanipulator (see Figure 1B). The 70 nm-thick W-VO_2 nanobelt achieved a maximum bending curvature of 0.33 μm^{-1}. Consequently, the maximum bending strain of the freestanding W-VO_2 film reached 1.1%, comparable to that of the freestanding VO_2 film.[43] This demonstrated that tungsten doping did not degrade the mechanical properties of the W-VO_2 film.

The MIT temperature of the freestanding W-VO_2 film could be changed by adjusting the atomic ratio of tungsten to vanadium elements. In this study, W-VO_2 films with different tungsten/vanadium atomic ratios were deposited on SiO_2 substrates using reactive sputtering of tungsten/vanadium alloy targets. Specifically, freestanding W-VO_2 films with atomic ratios of W/V of 0/100, 0.53/99.47, 0.86/99.14, and 1.6/98.4 were prepared and analyzed. The atomic ratios were confirmed by using energy-dispersive spectroscopy (EDS) and X-ray photoelectron spectroscopy (Figure S6). We noted that the results given by X-ray photoelectron spectroscopy (XPS) were slightly different from those given by EDS. EDS and XPS were both semiquantitative testing methods and could only analyze the surface of a sample. In addition to errors introduced by testing methods, the accuracy of tungsten content was also affected by the homogeneity of the sample, which included both in-plane uniformity and differences between the surface and the bulk of the sample. Therefore, the test results from EDS and XPS provided only a rough estimate of the tungsten content and illustrated the trend of changes in tungsten content among differently doped samples. To investigate the effect of tungsten doping on electrical properties, the freestanding W-VO_2 films were transferred to silicon nitride frames and their resistance as a function of temperature was measured (Figure 1C). The derivative logarithmic plots of resistance versus temperature for these films (Figure 1D) allowed us to determine the MIT temperatures. Specifically, the MIT temperatures for the W-VO_2 films with W/V atomic ratios of 0/100, 0.53/99.47, 0.86/99.14, and 1.6/98.4 were found to be 69 °C, 58.7 °C, 53 °C, and 40 °C, respectively. This indicated that for each 1% increase in tungsten doping, the MIT temperature decreased by approximately 18.1 °C. This adjustment rate of MIT temperature was lower than that reported in some studies.[52−54] When VO_2 was doped with W element, the reaction $2\ V^{4+} + W^{4+} \rightarrow 2\ V^{3+} + W^{6+}$ occurred, resulting in the formation of V^{3+}-W^{6+} and V^{3+}-V^{4+} pairs.[55] The appearance of V^{3+} in the system weakened the strong electron correlation, thus lowering the MIT temperature. In comparison, the doping effect of the pentavalent element was much weaker, half that of W. This was because the pentavalent element could only pair with one V^{3+}. In VO_2, oxygen vacancies were prevalent that could interact with W^{6+}, leading to the partial reduction of W^{6+} to W^{5+} for maintaining electrical neutrality.[56] Consequently, although the concentration of tungsten doping might be high, its effectiveness in modulating the MIT temperature was decreased. The resistance change ratios over different temperature ranges were measured: for VO_2 (2700 times from 20 to 90 °C), $W_{0.53\%}V_{99.47\%}O_2$ (230 times from 20 to 90 °C), $W_{0.86\%}V_{99.14\%}O_2$ (95 times from 20 to 70 °C), and $W_{1.6\%}V_{98.4\%}O_2$ (65 times from 20 to 50 °C). Comparing these results with those of W-VO_2 films grown on solid substrates (Table S2), we found that the phase-transition performance, in terms of electrical properties, of our freestanding W-VO_2 films is comparable to that of W-VO_2 films grown on solid substrates.

The X-ray diffraction (XRD) pattern of the freestanding W-VO_2 film transferred to a quartz substrate is presented in Figure S7A. The freestanding W-VO_2 film was oriented along the (011) plane of the VO_2 monoclinic phase, which matched the orientation of the W-VO_2 film grown directly on a quartz substrate. The temperature-dependent Raman spectra of the freestanding W-VO_2 film transferred to a quartz substrate were shown in Figure S7B. The intensity of the characteristic Raman peaks at 191 cm^{-1}, 221 cm^{-1}, 390 cm^{-1}, and 615 cm^{-1} gradually decreased with an increasing temperature. These peaks disappeared when the temperature exceeded 38 °C, signifying a phase transition of the W-VO_2 film. The surface

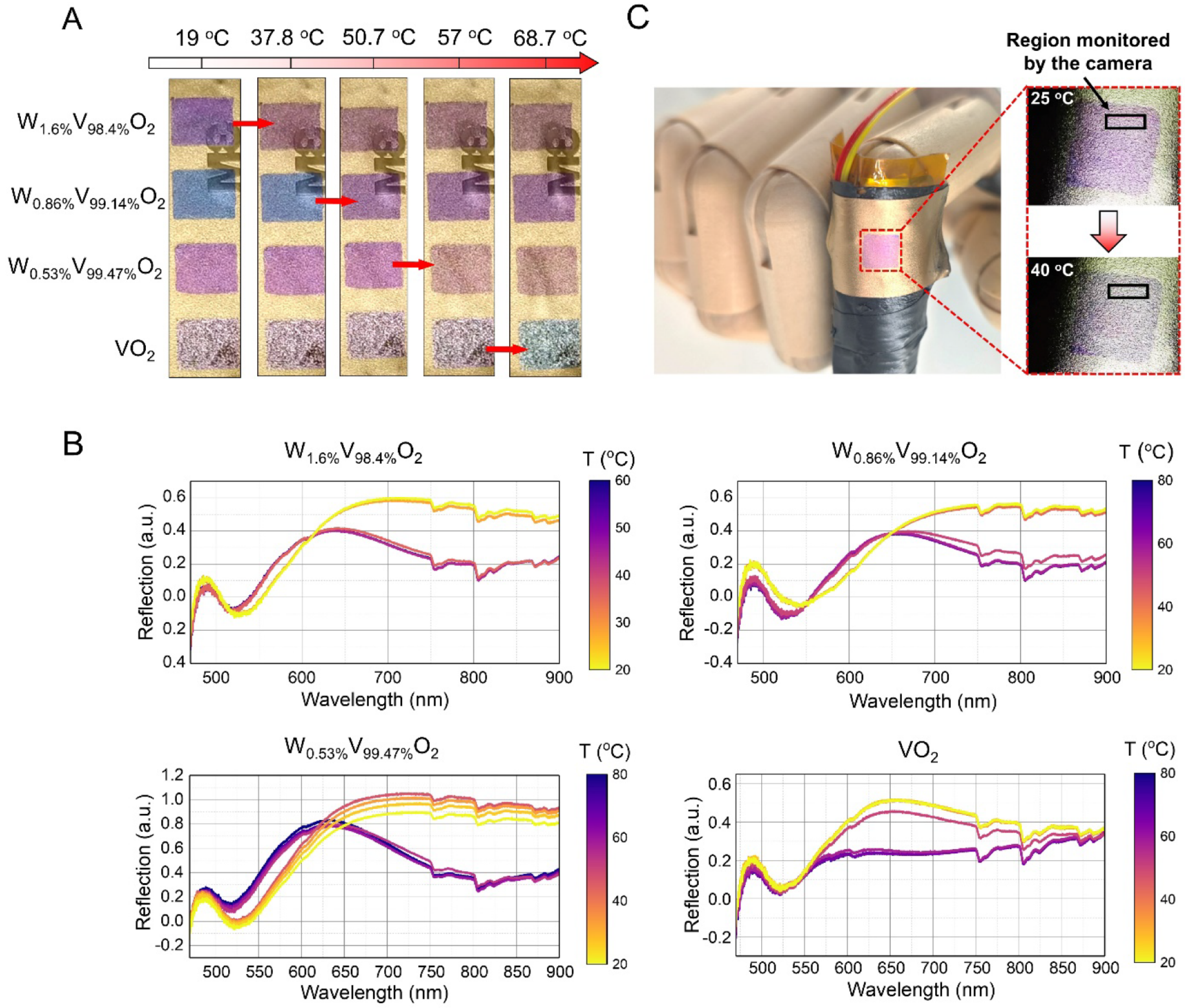

Figure 2. (A) Color change of W-VO_2 films with increasing temperature. (B) Reflection spectra of W-VO_2/Au-coated vinyl tapes at various temperatures. (C) Optical image of the thermochromic W-VO_2 tape attached to one finger of an artificial hand. The area of the $W_{1.6\%}V_{98.4\%}O_2$ tape monitored by the camera was highlighted by the black square. The color change of the $W_{1.6\%}V_{98.4\%}O_2$ tape was automatically identified by the computer.

morphology of the freestanding W-VO_2 film was characterized by using atomic force microscopy (AFM). As shown in Figure S8, the surface roughness of the transferred W-VO_2 film was 2.4 nm, which was almost identical to the roughness of the W-VO_2 film grown on a quartz substrate (2.3 nm). Therefore, the process of releasing and transferring the W-VO_2 film did not affect its crystal structure or surface morphology. The XRD pattern, Raman spectroscopy, and AFM analyses confirmed that the crystal structure, phase-transition behavior, and surface morphology of freestanding W-VO_2 films remained intact after transfer, affirming the reliability of the release and transfer process.

VO_2 films were widely utilized in active optical modulators across a broad wavelength spectrum, ranging from visible light to THz waves.[18,57] The temperature-driven working mechanism of these films implied that reducing the MIT temperature of a VO_2 film could significantly lower the power consumption of the optical modulator. To demonstrate the enhanced energy efficiency of W-VO_2 film-based optical modulators, we developed an electro-optical modulator using W-VO_2/CNT composite films (Figure S9A) and examined their electro-optical modulation properties. Two freestanding CNT films were cross-stacked on a quartz frame, and a freestanding W-VO_2 film (~110 nm thick) was subsequently transferred onto the CNT film to form the W-VO_2/CNT composite. Conductive graphite glue was applied to both ends of the W-VO_2/CNT film to serve as electrodes. For comparison, a VO_2/CNT film was prepared by using the same method. Figure S9B presents the transmission spectra of the W-VO_2/CNT and VO_2/CNT films under electrical stimulus, covering wavelengths from 400 to 2500 nm. Following the MIT driven by the applied voltage, the transmittance of the VO_2/CNT film at 1600 nm decreased from 45.3% to 6.5%, while the transmittance of the W-VO_2/CNT film decreased from 48.4% to 11.5%.

We further measured the transmittance changes of freestanding $W_{1.6\%}V_{98.4\%}O_2$/CNT and VO_2/CNT films with increasing electrical power density at 1600 nm. As shown in Figures 1E and S10, the driving power required for the phase transition of the freestanding $W_{1.6\%}V_{98.4\%}O_2$/CNT film was approximately 1.1 mW/mm^2, which was substantially lower than that of the freestanding VO_2/CNT film (~5.2 mW/mm^2). This indicated a significant reduction in power consumption for the $W_{1.6\%}V_{98.4\%}O_2$/CNT modulator com-

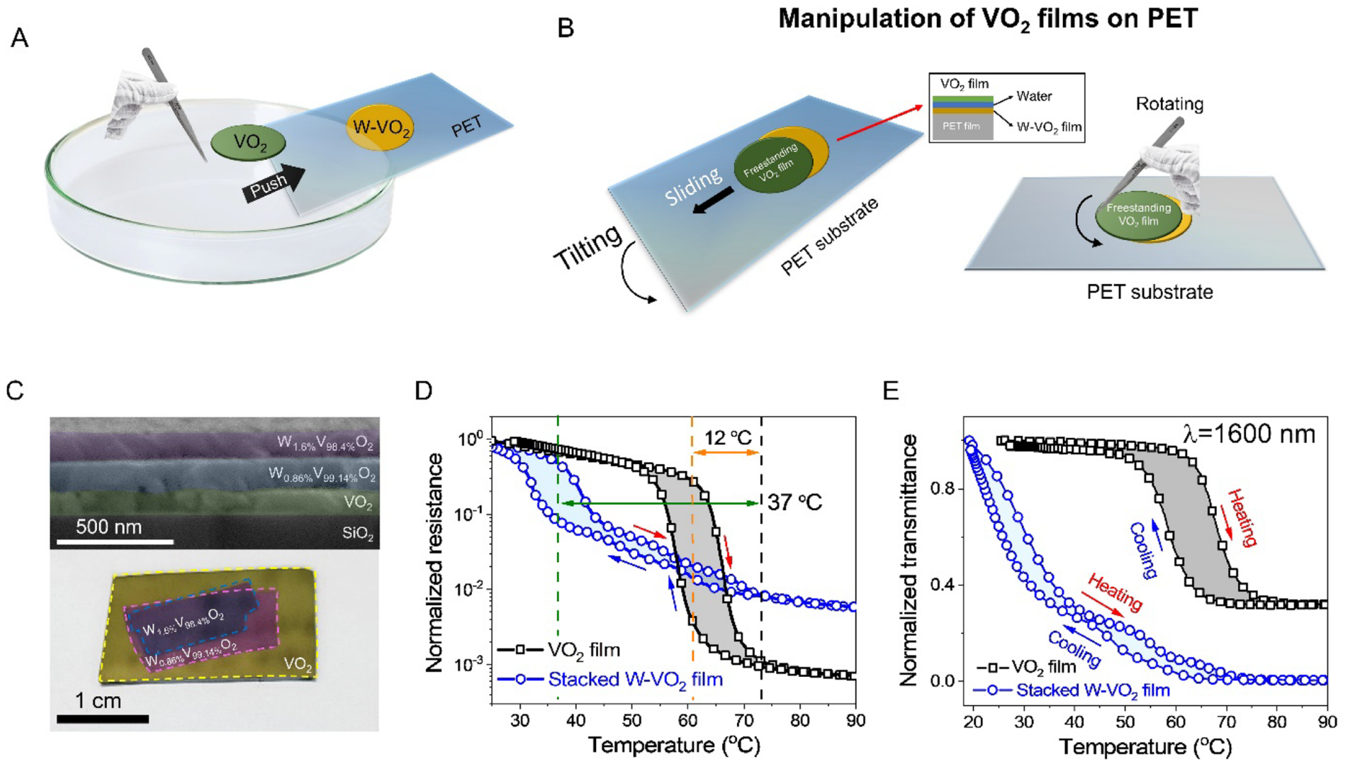

Figure 3. (A) Schematic illustration of the transferring and stacking process used to prepare a stacked W-VO$_2$ film. (B) Schematic representation showing the manipulation of the relative position and twist angle of the W-VO$_2$ film on a PET substrate. (C) Optical image of the stacked W-VO$_2$ film on a SiO$_2$/Si substrate. The top panel displayed an SEM image of the cross-section of the stacked W-VO$_2$ film. (D) R-T curves comparing the stacked W-VO$_2$ film with the VO$_2$ film. (E) Transmission-temperature curves for the stacked W-VO$_2$ film and the VO$_2$ film.

pared to the VO$_2$/CNT modulator. We also evaluated the transient response of the freestanding W$_{1.6\%}$V$_{98.4\%}$O$_2$/CNT film (Figure S11). The response time was defined as the duration for the electrical signal to change from 90% to 10%. The response time for the W$_{1.6\%}$V$_{98.4\%}$O$_2$/CNT film was approximately 32 ms, which was slightly longer than the response time of the VO$_2$/CNT film (~26 ms). The extended response time could be attributed to the smaller temperature difference between the W$_{1.6\%}$V$_{98.4\%}$O$_2$/CNT film and the environment.

The MIT characteristic of the W$_{1.6\%}$V$_{98.4\%}$O$_2$ film altered both the optical transmission and the thermal emissivity (thermal radiation) of the film. As a result, our W$_{1.6\%}$V$_{98.4\%}$O$_2$/CNT modulator had potential applications in infrared emissivity control and thermal coding, building on our previous research.[58] Currently, most approaches to thermal camouflage or thermal coding involved prepatterned designs that passively changed with environmental temperature (Table S3). However, these static, nonreconfigurable systems limited the versatility and potential applications of thermal coding. The high electrical conductivity and low thermal capacitance of the CNT film enabled active tuning of thermal radiation in the W-VO$_2$/CNT film with low power consumption (see discussion in the Supporting Information). This capability allowed each film to act as a dynamic pixel in an active thermal coding system. The reconfigurable nature of the electrically addressable optical modulator array facilitated the generation of arbitrary patterns, greatly enhancing the flexibility and applicability of thermal coding technology across various fields.

2.2. Thermochromism of Flexible W-VO$_2$ Films.

To better demonstrate the phase-transition properties and substrate adaptability of freestanding W-VO$_2$ films, we transferred the VO$_2$ film, W$_{0.53\%}$V$_{99.47\%}$O$_2$ film, W$_{0.86\%}$V$_{99.14\%}$O$_2$ film, and W$_{1.6\%}$V$_{98.4\%}$O$_2$ film onto 3 M^{TM} vinyl tape coated with a ~60 nm gold film, arranged from top to bottom in sequence. The four regions coated with these different W-VO$_2$ films displayed distinct colors. The thicknesses of VO$_2$, W$_{0.53\%}$V$_{99.47\%}$O$_2$, W$_{0.86\%}$V$_{99.14\%}$O$_2$, and W$_{1.6\%}$V$_{98.4\%}$O$_2$ films were 225, 75, 115, and 120 nm, respectively. The observed color differences could be attributed to two main factors: the varying thicknesses of the W-VO$_2$ films and the changes in the refractive index induced by element doping. The different film thicknesses created varying interference effects, while the doping altered the refractive index, contributing to the observed color variations.

As shown in Figure 2A, the W-VO$_2$ films on the tape exhibited color changes at specific temperatures: 37.8 °C for W$_{1.6\%}$V$_{98.4\%}$O$_2$, 50.7 °C for W$_{0.53\%}$V$_{99.47\%}$O$_2$, 57 °C for W$_{0.86\%}$V$_{99.14\%}$O$_2$, and 68.7 °C for VO$_2$. These color change temperatures corresponded closely with the MIT temperatures of the W-VO$_2$ films as determined by the R−T curves, confirming that the observed color transitions in Figure 2A were due to the MIT of the W-VO$_2$ films. Furthermore, we measured the temperature-dependent optical reflection spectra of these W-VO$_2$ films on Au-coated vinyl tape (Figure 2B). At the MIT point, the reflection spectrum valleys shifted toward shorter wavelengths. For example, in the W$_{1.6\%}$V$_{98.4\%}$O$_2$ film region, as the temperature exceeded 40 °C, the valley in the reflection spectrum shifted from 488 to 387 nm. This shift in the reflection spectra could be attributed to changes in the refractive index caused by MIT of the W-VO$_2$ films.

Thanks to its reversible thermochromic properties, W-VO_2 tapes could be employed as flexible temperature-indicating strips in wearable systems for monitoring temperature changes. To illustrate this application, we developed an automatic high-temperature alarm system using thermochromic W-VO_2 tape, demonstrated with a machine vision system. As shown in Figure 2C, a $W_{1.6\%}V_{98.4\%}O_2$ tape was attached to the finger of an artificial hand, which was heated using a polyimide heating plate. During the heating process, a camera continuously monitored the $W_{1.6\%}V_{98.4\%}O_2$ tape. When the temperature exceeded 40 °C, the tape's color shifted from bright purple to dark purple (Movie S3). This color change was automatically detected by the camera, triggering a high-temperature warning on the computer. The alarm temperature of the W-VO_2 tape could be fine-tuned by adjusting the tungsten-doped ratio of the W-VO_2 film. Unlike conventional thermocouples, the thermochromic W-VO_2 tape could conform more seamlessly to complex surfaces and cover a larger area. This meant that an overtemperature condition (e.g., 40 °C in the case of the $W_{1.6\%}V_{98.4\%}O_2$ tape shown in Figure 2C) anywhere within the covered area was immediately indicated by a color change.

2.3. Wafer-Scale Stacking of Freestanding W-VO_2 Films. Owing to the freestanding nature of W-VO_2 films, we were able to create multilayer W-VO_2 films using a layer-by-layer stacking technique (Figure 3A). Since no contaminants such as organic films were introduced during the transfer process, the surface of the freestanding W-VO_2 film was clean. Therefore, layer-by-layer stacking of freestanding W-VO_2 films was conducive to constructing vertically integrated W-VO_2 devices. First, a freestanding W-VO_2 (or VO_2) film was transferred onto a PET substrate. Once the W-VO_2/PET film had dried, it was subjected to an O_2 plasma treatment for 10 s to enhance its hydrophilicity. After this treatment, a second VO_2 (or W-VO_2) film was transferred onto the W-VO_2/PET substrate. The two-layer stacked W-VO_2 film was securely attached to the PET substrate and allowed to dry thoroughly in the air. As shown in Figure S13, a $W_{1.6\%}V_{98.4\%}O_2$ film, with an approximate area of 10 cm^2, was successfully stacked onto a VO_2/PET substrate using this layer-by-layer stacking method.

When we initially transferred the VO_2 film onto the W-VO_2/PET substrate from water, the water beneath the VO_2 layer acted as a lubricant, creating a separation between the VO_2 layer and the W-VO_2/PET substrate. This allowed the VO_2 layer to slide on the W-VO_2/PET substrate when the PET substrate was tilted. Consequently, we could control the relative position between the adjacent VO_2 layers by manipulating the PET substrate (see Movie S4). Additionally, we adjusted the twist angle between the adjacent VO_2 layers (see Movie S5). As shown in Figures 3B and S14, the VO_2 layer shifted to the left and upward sides of the W-VO_2 layer when the PET substrate was tilted in those respective directions. Furthermore, we rotated the top VO_2 layer by 35° relative to the bottom W-VO_2 layer, as demonstrated in Figures 3B and S14. Utilizing this wafer-scale transfer and layer-by-layer stacking technique, we successfully prepared a three-layer stacked W-VO_2/PET film with a $W_{0.53\%}V_{99.47\%}O_2$/VO_2/$W_{0.53\%}V_{99.47\%}O_2$ structure (Figure S14).

The sharp phase transition around the MIT temperature enabled VO_2 films to switch readily between insulating and metallic states.[59] However, maintaining a state between insulator and metal poses a significant challenge.[9] At the precise MIT point, VO_2 films became highly sensitive to external stimuli, a sensitivity that substantially diminished when the temperature deviated from the MIT point. Achieving accurate temperature control near the MIT point requires a sophisticated temperature control system, which demanded high power consumption and added to the device complexity. Therefore, broadening the MIT region of the VO_2 films was highly desirable. Tang et al. had shown that multilayer W-VO_2 films with varying tungsten-doped concentrations, deposited on a glass substrate, could achieve an extended MIT region.[9] However, this direct-growth method was unsuitable for nonheat-resistant flexible substrates. In our work, we employed a layer-by-layer stacking technique to construct a gradient tungsten-doped VO_2 film, which offers significant advantages in terms of substrate adaptability compared with the direct-growth method.

As shown in Figure 3C, we transferred $W_{0.86\%}V_{99.14\%}O_2$ and $W_{1.6\%}V_{98.4\%}O_2$ onto a VO_2/SiO_2/Si substrate to construct a gradient tungsten-doped VO_2 film. Compared with flexible substrates such as PI and PET films, the SiO_2/Si substrate exhibited higher thermal conductivity, facilitating temperature equilibrium during changes. Therefore, the preparation of the stacked W-VO_2 film on the solid substrate facilitated precise measurement of its electrical property under various temperatures. The cross-sectional image of the stacked W-VO_2 film, shown in the upper panel of Figure 3C, revealed the fine interfaces between the three layers.

We measured the resistance−temperature (R−T) curve of the stacked W-VO_2 film. As shown in Figure 3D, the MIT width of the stacked W-VO_2 film was broadened to approximately 37 °C, compared to the relatively narrow MIT width (~12 °C) of the VO_2 film. Moreover, the stacked W-VO_2 film exhibited a significantly reduced hysteresis. For instance, at 60 °C, the ratio of $R_{\text{heating}}/R_{\text{cooling}}$ for the VO_2 film was ~60, while for the stacked W-VO_2 film it was just 1.13. The resistance change ratio from 20 to 90 °C for the stacked W-VO_2 film exceeded 2 orders of magnitude, comparable to that achieved using the direct-growth method (Table S2). We also measured the transmission-temperature curve of the stacked W-VO_2 film at a wavelength of 1600 nm (Figure 3E). This measurement further confirmed that the MIT region of the stacked W-VO_2 film was significantly broader than that of the VO_2 film with much smaller hysteresis. These properties made the stacked W-VO_2 film an excellent candidate for use in temperature-sensitive applications such as uncooled thermal detectors,[60] benefiting from both its broad MIT range and minimal hysteresis.

2.4. Multistate Infrared Camouflage Films and Nonreciprocal Ultrafast Light Modulators. To demonstrate the potential applications of stacked W-VO_2 films in the optical field, we developed both infrared camouflage devices based on three-layer stacked W-VO_2 films and nonreciprocal ultrafast light modulators utilizing VO_2/Mica/$W_{1.6\%}V_{98.4\%}O_2$ films. Infrared camouflage, a technique for deceiving infrared cameras by altering an object's thermal radiation, holds significant importance in various military applications.[9,61] According to the Stefan−Boltzmann law, an object's thermal radiation was determined by its emissivity and temperature. Thus, adjusting emissivity provided an efficient method to manipulate an object's thermal radiation, achieving infrared camouflage. MIT in VO_2 films led to significant changes in emissivity, making these films ideal for infrared camouflage. Additionally, advances in tungsten doping and multiple lithography techniques have evolved VO_2-based infrared camouflage devices from dual-state to multistate capabilities.[62]

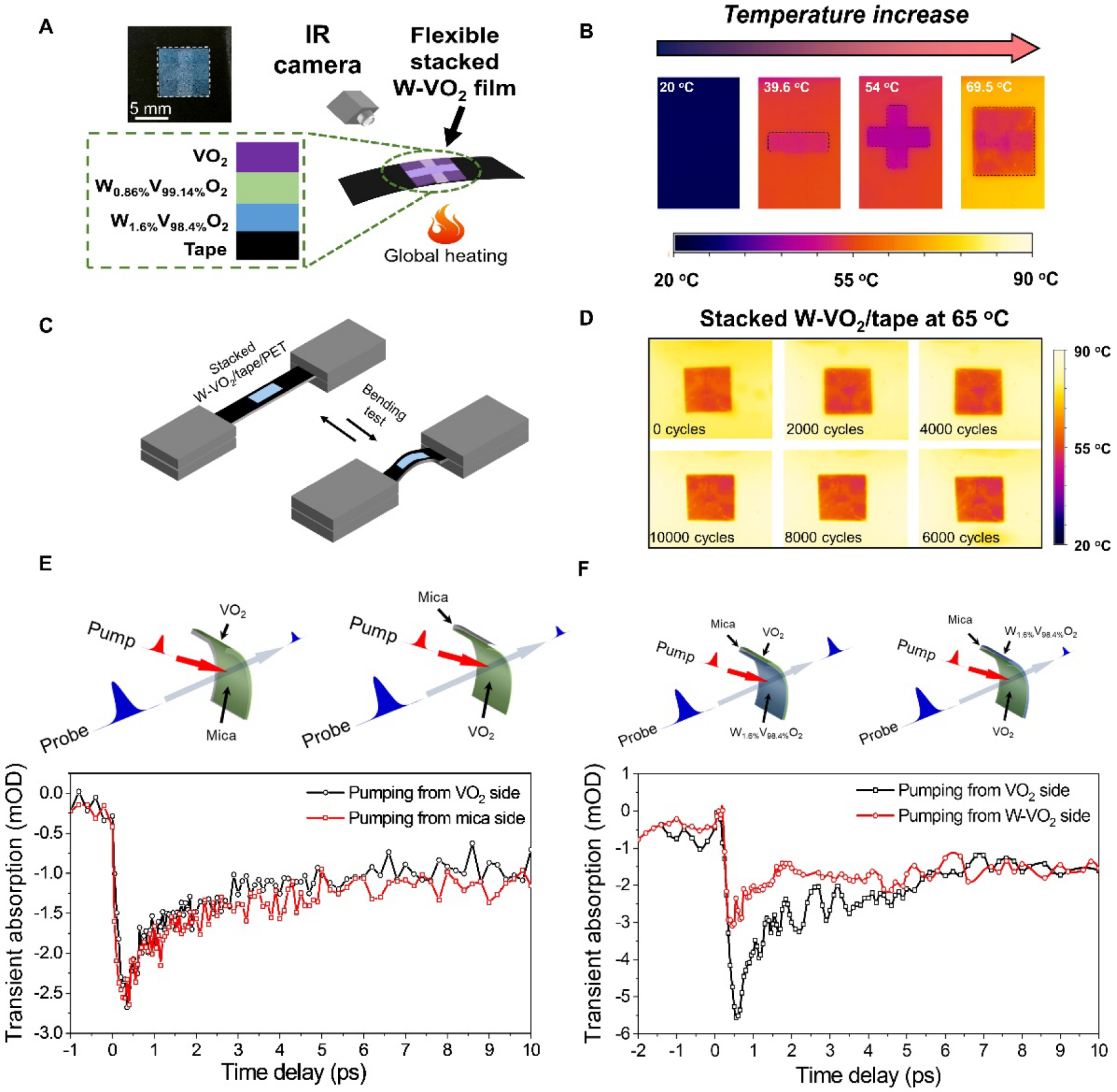

Figure 4. (A) Schematic illustration of infrared camouflage devices based on the three-layer stacked W-VO$_2$ film. The inset displays an optical image of the three-layer stacked W-VO$_2$ film transferred onto black vinyl tape. (B) Infrared images depicting the changes in temperature for the three-layer stacked W-VO$_2$ film. (C) Schematic illustration of the bending test for the stacked W-VO$_2$/tape. (D) Infrared images of the stacked W-VO$_2$/tape at 65 °C after bending cycles of 0, 2000, 4000, 6000, 8000, and 10,000 under a curvature of 57 m^{-1}. (E) Transient absorption spectra of the VO$_2$/mica film, obtained by pumping (λ_{pump} = 800 nm) and probing (λ_{probe} = 1178 nm) from both the VO$_2$ and mica sides. (F) Transient absorption spectra of the VO$_2$/mica/W$_{1.6\%}$V$_{98.4\%}$O$_2$ film, obtained by pumping (λ_{pump} = 800 nm) and probing (λ_{probe} = 1178 nm) from both the VO$_2$ side and the W$_{1.6\%}$V$_{98.4\%}$O$_2$ side with a fluence of 0.9 μJ/mm^2.

Infrared camouflage devices typically required flexible covering for the object's surface, making flexibility a crucial characteristic. The high-temperature deposition (>450 °C) of VO$_2$ films had limited the preparation of VO$_2$ infrared camouflage devices to solid substrates or a few high-temperature-resistant flexible ones. In this study, we successfully transferred and layered three W-VO$_2$ films (W$_{1.6\%}$V$_{98.4\%}$O$_2$ film, W$_{0.86\%}$V$_{99.14\%}$O$_2$ film, and VO$_2$ film) onto 3M^{TM} vinyl tape, creating a temperature-responsive, flexible, polymorphic infrared camouflage device. As illustrated in Figures 4A and S15, we first placed a rectangular W$_{1.6\%}$V$_{98.4\%}$O$_2$ strip (7 × 2 mm^2) at the bottom. This was followed by layering a rectangular W$_{0.86\%}$V$_{99.14\%}$O$_2$ strip (7 × 2 mm^2) in the middle, and finally, covering the top surface with a square VO$_2$ film (7 × 7 mm^2). Using an infrared camera, we observed infrared imaging of the stacked W-VO$_2$ films. At room temperature, due to the emissivity of the stacked W-VO$_2$ films matching the surrounding environment, no image was visible on the infrared camera (Figure 4B and Movie S6). When the temperature exceeded 39.6 °C, the phase transition of the W$_{1.6\%}$V$_{98.4\%}$O$_2$ strip reduced its emissivity, creating an infrared temperature difference between the strips and its surroundings. As the temperature climbed to 54 °C, the phase transition of the W$_{0.86\%}$V$_{99.14\%}$O$_2$ film occurred, causing the vertically oriented W$_{0.86\%}$V$_{99.14\%}$O$_2$ strip to appear in the infrared image. This formed a cross-pattern with the existing horizontally oriented W$_{1.6\%}$V$_{98.4\%}$O$_2$ strip. Finally, when the temperature rose beyond 69.5 °C, the square VO$_2$ film became visible, masking the underlying cross structure of the W$_{1.6\%}$V$_{98.4\%}$O$_2$ and W$_{0.86\%}$V$_{99.14\%}$O$_2$ strips.

The infrared images of the stacked W-VO$_2$/tape at 65 °C were captured after subjecting the sample to 0, 2000, 4000, 6000, 8000, and 10,000 bending cycles under a curvature of 57 m^{-1} (Figure 4C). Throughout the bending test, the stacked W-

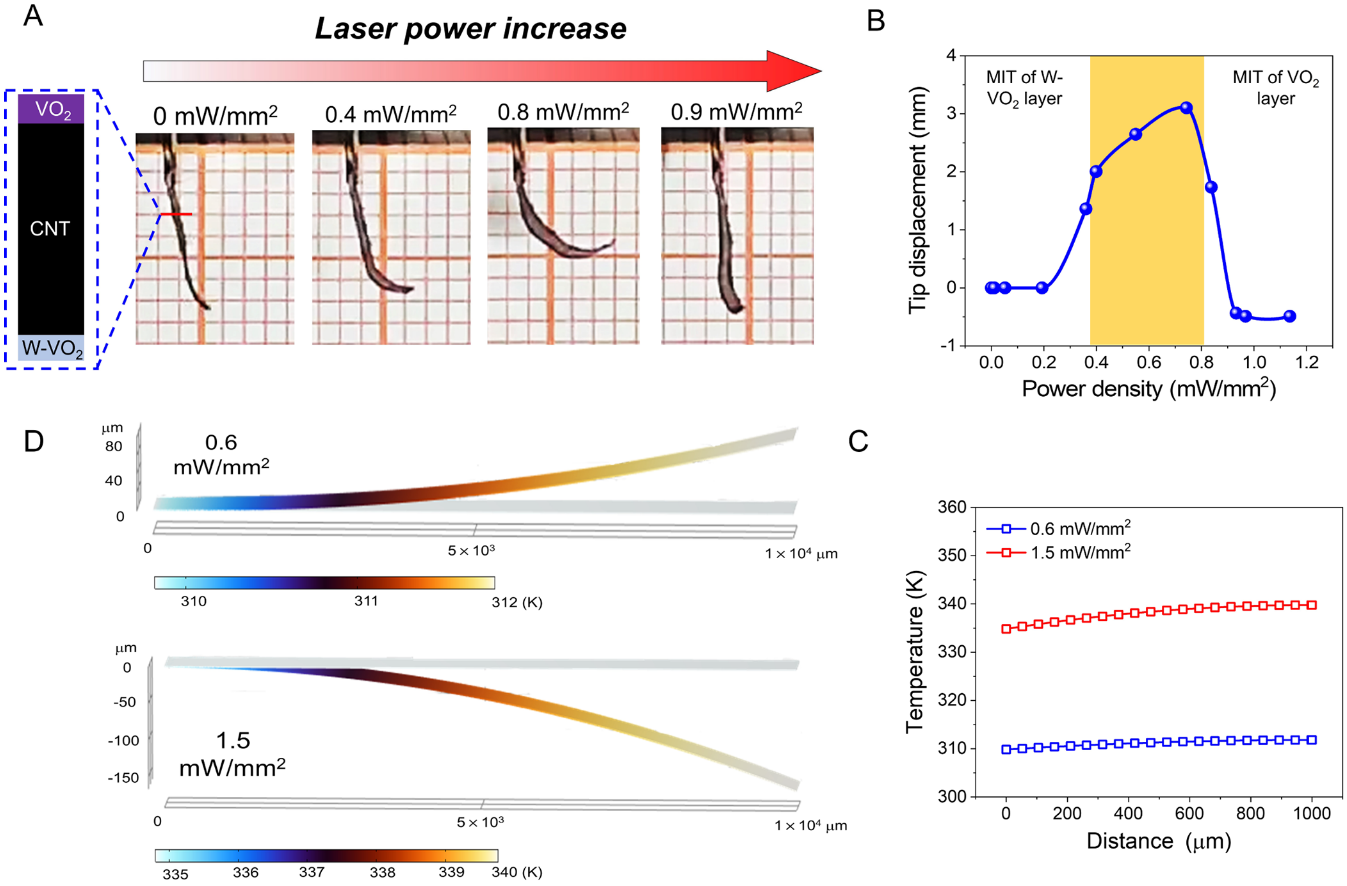

Figure 5. (A) Optical images of the $W_{1.6\%}V_{98.4\%}O_2$/CNT/VO_2 photoactuator under laser irradiation with different laser power density. (B) Deformation of the $W_{1.6\%}V_{98.4\%}O_2$/CNT/VO_2 photoactuator under different laser power density. (C) Simulated temperature distribution and (D) deformation of the $W_{1.6\%}V_{98.4\%}O_2$/CNT/VO_2 photoactuator under the laser irradiation with the power density of 0.6 mW/mm^2 and 1.5 mW/mm^2.

VO_2/tape was securely attached to a PET film. Remarkably, the infrared images taken at various bending intervals showed minimal differences, suggesting that the phase-transition properties of the stacked W-VO_2 film remained consistent (Figure 4D). This consistent performance underscored the excellent flexibility of the stacked W-VO_2 film, making it suitable for covering complex surfaces and thereby meeting the practical demands of infrared camouflage devices.

VO_2 was a potential candidate for an ultrafast optical switch due to its ability to undergo an ultrafast MIT when excited by femtosecond laser pulses.[63,64] When operating in transmission mode and the substrate was transparent to the pumping light, the ultrafast photoresponse of VO_2 was always reciprocal. For instance, we measured the VO_2/mica ultrafast photoresponse characteristics using a pump−probe system, as shown in Figure S16. The transient absorption (TA) spectrum by pumping from the VO_2 side was nearly identical to that pumped from the mica side (Figure 4E). Figure 4F shows transient absorption spectra of VO_2/mica/$W_{1.6\%}V_{98.4\%}O_2$ pumped from the VO_2 side and from the $W_{1.6\%}V_{98.4\%}O_2$ side. In Figure 4F, we found that the TA spectrum by pumping from the VO_2 side (TA_VO_2) differed from that pumped from the $W_{1.6\%}V_{98.4\%}O_2$ side (TA_W-VO_2) under the fluence of 0.9 μJ/mm^2. Specifically, the extinction of TA_VO_2 was 1.8 times higher than that of TA_W-VO_2, allowing for a greater modulation depth when pumping from the VO_2 side. We normalized the spectra of TA_VO_2 and TA_W-VO_2 and compared the recovery times of the VO_2 film and the $W_{1.6\%}V_{98.4\%}O_2$ film (Figure S17). Before 2 ps, the dynamic processes experienced by the VO_2 film and the $W_{1.6\%}V_{98.4\%}O_2$ film were almost identical. In contrast, after 2 ps, the signal of TA_VO_2 continued to slowly decrease and returned to the initial state after ∼40 ps. In contrast, the signal of TA_W-VO_2 remained almost unchanged after two picoseconds. This was because the MIT temperature of the $W_{1.6\%}V_{98.4\%}O_2$ film was only 40 °C, and laser irradiation increases the film's temperature, preventing the signal of TA_W-VO_2 from fully recovering to its initial state.

2.5. Photoactuator with "Band-Pass" Property. VO_2 was a promising material for creating high-performance photoactuators because it undergoes a significant structural phase change when exposed to light and is compatible with strong light-absorbing materials like CNTs.[22,65] When stimulated by light, VO_2-based actuators bend toward the VO_2 side due to the shrinkage of VO_2 along its c_R axis. After the structural change of VO_2, the deformation of the VO_2-based actuators becomes much smaller, even with increased light power. Light with power higher than the actuator's triggering threshold can pass through when used as mechanical light modulators, such as in smart curtains. However, if the light is too strong, the smart curtain should limit the light that passes spontaneously for protection.

Herein, we have developed a photoactuator using a $W_{1.6\%}V_{98.4\%}O_2$/CNT/VO_2 film as the base. The W-VO_2 film

(~120 nm) and VO_2 film (~120 nm) were transferred onto the front and back sides of the CNT film, which had a thickness of approximately 1.5 μm. The photoresponsive behavior of the rectangular $W_{1.6\%}V_{98.4\%}O_2$/CNT/VO_2 film is shown in Figure 5A,B. When the laser power exceeded 0.2 mW/mm^2, the $W_{1.6\%}V_{98.4\%}O_2$/CNT/VO_2 film bent sharply toward the W-VO_2 side due to the MIT of W-VO_2, resulting in an increase in tip displacement from 0 mm to 2 mm. As the laser power increased from 0.4 to 0.8 mW/mm^2, the slope of the displacement versus the laser power decreased significantly, signifying the completion of the phase transition of W-VO_2. At a laser power of 0.8 mW/mm^2, the $W_{1.6\%}V_{98.4\%}O_2$/CNT/VO_2 film bent toward the VO_2 side due to the MIT of VO_2 and almost returned to its original state. We conducted a finite element simulation to model the deformation of the $W_{1.6\%}V_{98.4\%}O_2$/CNT/VO_2 film under light stimuli (see Figure S18 for detailed simulation method and parameters). As shown in Figure 5C, when the irradiated light power was 0.6 mW/mm^2, the maximum temperature of the $W_{1.6\%}V_{98.4\%}O_2$/CNT/VO_2 film reached 312 K. This temperature increase triggered the MIT of the $W_{1.6\%}V_{98.4\%}O_2$ layer, causing the $W_{1.6\%}V_{98.4\%}O_2$/CNT/VO_2 film to bend toward the W-VO_2 side (Figure 5D). As the light power rose to 1.5 mW/mm^2, the maximum temperature of the $W_{1.6\%}V_{98.4\%}O_2$/CNT/VO_2 film increased to 340 K (Figure 5C), inducing the MIT of the VO_2 layer and resulting in the $W_{1.6\%}V_{98.4\%}O_2$/CNT/VO_2 film bending toward the VO_2 side (Figure 5D).

3. CONCLUSION

We have successfully developed wafer-scale freestanding W-VO_2 films with tailored phase-transition temperatures. By varying the tungsten-doped concentrations, we could effectively fine-tune the phase-transition properties of the VO_2 film. These freestanding W-VO_2 films could be seamlessly transferred to any flexible substrate, maintaining excellent phase-transition performance in both optical and electrical characteristics. Our research demonstrated that flexible W-VO_2 films could serve as flexible temperature-indicating strips, multistate infrared camouflage devices, nonreciprocal ultrafast light modulators, and smart photoactuators. The potential applications of freestanding W-VO_2 films were vast and largely unexplored, opening opportunities for their integration with other functional materials to create innovative solutions. Further investigation into the diverse applications of freestanding W-VO_2 films was highly encouraged to unlock their full potential.

4. EXPERIMENTAL METHOD AND MATERIAL CHARACTERIZATION

4.1. Synthesis of W-VO_2 Films. W-VO_x films were deposited on SiO_2 substrates (quartz or SiO_2/Si substrates) via reactive magnetron sputtering. Sputtering was conducted in a flowing gas mixture with a flow rate of 50 standard cubic centimeter per minute (sccm) (31−33 sccm of Ar and 17−19 sccm of 96% Ar/4% O_2 depending on the environmental humidity and temperature). The sputtering pressure was 0.6 Pa, and the sputtering power was 55 W. The thickness of the W-VO_x film was controlled by the sputtering time. The W-VO_x film was annealed at a temperature of 450 °C for 10 min in a low-pressure oxygen atmosphere (4.5 Pa).

4.2. Preparation of VO_2/mica/$W_{1.6\%}V_{98.4\%}O_2$ Films and VO_2/CNT/$W_{1.6\%}V_{98.4\%}O_2$ Films. Freestanding VO_2 films and freestanding $W_{1.6\%}V_{98.4\%}O_2$ films were prepared by the NPE method. Then, the VO_2 film was transferred onto one side of the mica film. After the VO_2/mica film was dried, the freestanding $W_{1.6\%}V_{98.4\%}O_2$ film was transferred onto the other side of the mica film. The preparation of the VO_2/CNT/$W_{1.6\%}V_{98.4\%}O_2$ film was very similar to that of the VO_2/mica/$W_{1.6\%}V_{98.4\%}O_2$ film. Freestanding VO_2 films and freestanding $W_{1.6\%}V_{98.4\%}O_2$ films were prepared using the NPE method. Then, the VO_2 film was transferred from water onto one side of the CNT film. The CNT film was treated with oxygen plasma to enhance its hydrophilicity. After the VO_2/CNT film was dried, the freestanding $W_{1.6\%}V_{98.4\%}O_2$ film was transferred onto the other side of the CNT film.

4.3. Material Characterization and Performance Testing. SEM images were taken using a JEOL JSM-6510 scanning electron microscope and an FEI Nova 450 scanning electron microscope. TEM images were taken using an FEI Tecnai F20 transmission electron microscope. XPS measurements were performed using a Thermo Scientific^{TM} ESCALAB 250Xi. XRD measurements were performed using a Rigaku Smartlab. Raman spectroscopy and AFM measurements were performed by using the WITec alpha 300 system. The performance of the VO_2/CNT electro-optical modulator was measured using a spectrometer (Hitachi U-4100). The R-T curves of the VO_2 films were measured using a probe station (Cascade M150), a homemade temperature-controlling system, and a source meter (Keysight B2902A). The reflection spectra of thermochromic W-VO_2 tapes were measured using a homemade optical reflection measuring system comprising a halogen lamp (HL2000), an optical spectrometer (Ocean optics USB4000), and a temperature controller (Lakeshore 335). The infrared images of the stacked W-VO_2 film were taken by an infrared camera (Optris 640).

ASSOCIATED CONTENT

Data Availability Statement

All the data used in this article and Supporting Information are provided, and any data deemed relevant can be obtained from the corresponding authors.

Supporting Information

The Supporting Information is available free of charge at https://pubs.acs.org/doi/10.1021/acsnano.4c15059.

> SEM image of the $W_{1.6\%}V_{98.4\%}O_2$ film grown on a quartz substrate; TEM image of the freestanding $W_{1.6\%}V_{98.4\%}O_2$ film; electron diffraction pattern of the freestanding $W_{1.6\%}V_{98.4\%}O_2$ film; optical image of a freestanding $W_{1.6\%}V_{98.4\%}O_2$ film floating on water; optical image of a $W_{1.6\%}V_{98.4\%}O_2$ film transferred onto a PET substrate; Optical image of the $W_{1.6\%}V_{98.4\%}O_2$/PET film with a curvature of 1/0.95 mm^{-1}; transmittance of the $W_{1.6\%}V_{98.4\%}O_2$/PET film, both before and after the bending test; comparison of bending strain across various devices utilizing (doped) VO_2; optical image of the $W_{1.6\%}V_{98.4\%}O_2$/mica film; transmittances of the $W_{1.6\%}V_{98.4\%}O_2$/mica film with different temperatures; modulation amplitude and MIT temperature of the $W_{1.6\%}V_{98.4\%}O_2$/mica film as a function of the number of bending cycles; XPS of W-VO_2 films; comparison of the resistance change ratio between freestanding W-VO_2 films and W-VO_2 films grown on solid substrates; XRD and Raman spectra of the $W_{1.6\%}V_{98.4\%}O_2$ film; optical and AFM images of the freestanding

$W_{1.6\%}V_{98.4\%}O_2$ film transferred onto a quartz substrate; optical and AFM images of the $W_{1.6\%}V_{98.4\%}O_2$ film grown on a quartz substrate; optical image and transmittance of the freestanding $W_{1.6\%}V_{98.4\%}O_2$/CNT film; simulated temperature distribution image of a freestanding VO_2/CNT film and a W-VO_2/CNT/quartz; schematic diagram of the electro-optical measurement system and transient response of the W-VO_2/CNT film and the VO_2/CNT film; comparison of the thermal camouflage devices using (doped) VO_2; schematic diagram for reducing maintenance energy through the hysteresis effect of VO_2; optical image of the $W_{1.6\%}V_{98.4\%}O_2$/VO_2/PET film; optical images of manipulating W-VO_2 films' position and the three-layer stacked W-VO_2/PET film with a $W_{0.53\%}V_{99.47\%}O_2$/VO_2/$W_{0.53\%}V_{99.47\%}O_2$ structure; schematic diagram for patterned stacking of W-VO_2 films; schematic diagram of the pump−probe system; normalized transient absorption spectra of the VO_2/mica/$W_{1.6\%}V_{98.4\%}O_2$ film; geometrical model of the $W_{1.6\%}V_{98.4\%}O_2$/CNT/VO_2 film; and material properties used in the photo-actuating simulation of the $W_{1.6\%}V_{98.4\%}O_2$/CNT/VO_2 film (PDF)

Movie 1: Releasing a W-VO_2 film using NPE technique and transferring a freestanding W-VO_2 film from water to PET film (MP4)

Movie 2: Freestanding VO_2 and W-VO_2 films on PET films (MP4)

Movie 3: Automatic recognition of thermochromism of flexible W-VO_2 films (MP4)

Movie 4: Manipulating freestanding W-VO_2 film on PET film (MP4)

Movie 5: Rotating freestanding W-VO_2 film on PET film (MP4)

Movie 6: Multistate infrared camouflage (MP4)

Thermal simulation file 1 (ZIP)

Thermal simulation file 2 (ZIP)

AUTHOR INFORMATION

Corresponding Authors

He Ma − *Institute of Information Photonics Technology and School of Physics and Optoelectronic Engineering, Beijing University of Technology, Beijing 100124, P.R. China;* orcid.org/0000-0002-1976-2641; Email: mahe_beijing@bjut.edu.cn

Kai Liu − *State Key Laboratory of New Ceramics and Fine Processing, School of Materials Science and Engineering, Tsinghua University, Beijing 100084, P.R. China;* orcid.org/0000-0002-0638-5189; Email: liuk@tsinghua.edu.cn

Xinping Zhang − *Institute of Information Photonics Technology and School of Physics and Optoelectronic Engineering, Beijing University of Technology, Beijing 100124, P.R. China;* orcid.org/0000-0001-6534-0004; Email: zhangxinping@bjut.edu.cn

Authors

Yuan Li − *Institute of Information Photonics Technology and School of Physics and Optoelectronic Engineering, Beijing University of Technology, Beijing 100124, P.R. China*

Run Shi − *State Key Laboratory of New Ceramics and Fine Processing, School of Materials Science and Engineering, Tsinghua University, Beijing 100084, P.R. China;* orcid.org/0000-0002-3214-4661

Yonghuang Wu − *State Key Laboratory of New Ceramics and Fine Processing, School of Materials Science and Engineering, Tsinghua University, Beijing 100084, P.R. China*

Shifeng Feng − *Institute of Information Photonics Technology and School of Physics and Optoelectronic Engineering, Beijing University of Technology, Beijing 100124, P.R. China*

Yulan Fu − *Institute of Information Photonics Technology and School of Physics and Optoelectronic Engineering, Beijing University of Technology, Beijing 100124, P.R. China;* orcid.org/0000-0002-1705-4246

Yuanqi Wei − *State Key Laboratory of Low-Dimensional Quantum Physics, Department of Physics, Collaborative Innovation Center of Quantum Matter, Tsinghua University, Beijing 100084, P.R. China*

Xuzhe Zhao − *Tsinghua-Berkeley Shenzhen Institute, Institute of Data and Information, Tsinghua Shenzhen International Graduate School, Tsinghua University, Shenzhen 518055, P.R. China*

Kaichen Dong − *Tsinghua-Berkeley Shenzhen Institute, Institute of Data and Information, Tsinghua Shenzhen International Graduate School, Tsinghua University, Shenzhen 518055, P.R. China;* orcid.org/0000-0001-5334-4243

Kaili Jiang − *State Key Laboratory of Low-Dimensional Quantum Physics, Department of Physics, Collaborative Innovation Center of Quantum Matter, Tsinghua University, Beijing 100084, P.R. China*

Complete contact information is available at: https://pubs.acs.org/10.1021/acsnano.4c15059

Author Contributions

H.M., X.P.Z., and K.L. conceived the project. Y.L. prepared tungsten-doped VO_2 films and multilayer stacked W-VO_2 films, and measured the electrical, optical, and mechanical properties of the films. Y.Q.W., K.L.J., and H.M. measured the mechanical properties of W-VO_2 films using in situ electron microscopy. Y.L., R.S., and Y.H.W. measured the infrared property of the W-VO_2 film. S.F.F. and Y.L.F. measured the transient absorption spectra. Y.L. measured the actuation performance of the photoactuator. H.M. and Y.L. wrote the manuscript. K.L., K.C.D., and X.P.Z. revised the manuscript. All authors discussed the manuscript and provided suggestions for revision.

Notes

The authors declare no competing financial interest.

ACKNOWLEDGMENTS

H.M. acknowledges support from the National Natural Science Foundation of China (Grant No. 52272286), Beijing Natural Science Foundation (Grant No. Z2006E01202301), and Beijing Nova Program (No. Z20110006820111). H.M. and K. D. acknowledge support from the National Key R&D Program of China (Grant No. 2023YFB3208700). X.Z. acknowledges support from the National Natural Science Foundation of China (Grant No. 61735002). K.L. acknowledges support from the Basic Science Center Project of NSFC (Grant No. 52388201) and the National Natural Science Foundation of China (Grant No. 52272041).

REFERENCES

(1) Li, S.; Tian, M.; Gao, Q.; Wang, M.; Li, T.; Hu, Q.; Li, X.; Wu, Y. Nanometre-thin indium tin oxide for advanced high-performance electronics. *Nat. Mater.* **2019**, *18* (10), 1091.

(2) Shin, J.; Jeong, B.; Kim, J.; Nam, V. B.; Yoon, Y.; Jung, J.; Hong, S.; Lee, H.; Eom, H.; Yeo, J. Sensitive wearable temperature sensor with seamless monolithic integration. *Adv. Mater.* **2020**, *32* (2), 1905527.

(3) Brousse, K.; Pinaud, S.; Nguyen, S.; Fazzini, P.-F.; Makarem, R.; Josse, C.; Thimont, Y.; Chaudret, B.; Taberna, P.-L.; Respaud, M.; et al. Facile and scalable preparation of ruthenium oxide-based flexible micro-supercapacitors. *Adv. Energy Mater.* **2020**, *10* (6), 1903136.

(4) Zheng, L.; Teng, F.; Ye, X.; Zheng, H.; Fang, X. Photo/electrochemical applications of metal sulfide/TiO_2 heterostructures. *Adv. Energy Mater.* **2020**, *10* (1), 1902355.

(5) Kumar, S.; Pickett, M. D.; Strachan, J. P.; Gibson, G.; Nishi, Y.; Williams, R. S. Local temperature redistribution and structural transition during joule-heating-driven conductance switching in VO_2. *Adv. Mater.* **2013**, *25* (42), 6128−6132.

(6) Lee, D.; Chung, B.; Shi, Y.; Kim, G. Y.; Campbell, N.; Xue, F.; Song, K.; Choi, S. Y.; Podkaminer, J. P.; Kim, T. H. Isostructural metal-insulator transition in VO_2. *Science* **2018**, *362* (6418), 1037.

(7) O'Callahan, B. T.; Jones, A. C.; Park, J. H.; Cobden, D. H.; Atkin, J. M.; Raschke, M. B. Inhomogeneity of the ultrafast insulator-to-metal transition dynamics of VO_2. *Nat. Commun.* **2015**, *6*, 6849.

(8) Li, G.; Xie, D.; Zhong, H.; Zhang, Z.; Fu, X.; Zhou, Q.; Li, Q.; Ni, H.; Wang, J.; Guo, E. Photo-induced non-volatile VO_2 phase transition for neuromorphic ultraviolet sensors. *Nat. Commun.* **2022**, *13* (1), 1729.

(9) Tang, K.; Wang, X.; Dong, K.; Li, Y.; Li, J.; Sun, B.; Zhang, X.; Dames, C.; Qiu, C.; Yao, J.; et al. A Thermal Radiation Modulation Platform by Emissivity Engineering with Graded Metal−Insulator Transition. *Adv. Mater.* **2020**, *32* (36), 1907071.

(10) Xue, W.; Liu, G.; Zhong, Z.; Dai, Y.; Shang, J.; Liu, Y.; Yang, H.; Yi, X.; Tan, H.; Pan, L.; et al. A 1D Vanadium Dioxide Nanochannel Constructed via Electric-Field-Induced Ion Transport and its Superior Metal−Insulator Transition. *Adv. Mater* **2017**, *29* (39), 1702162.

(11) Zheng, J.; Bao, S.; Jin, P. $TiO_2(R)/VO_2(M)/TiO_2(A)$ multilayer film as smart window: combination of energy-saving, antifogging and self-cleaning functions. *Nano Energy* **2015**, *11*, 136−145.

(12) Jian, J.; Wang, X.; Li, L.; Fan, M.; Zhang, W.; Huang, J.; Qi, Z.; Wang, H. Continuous tuning of phase transition temperature in VO_2 thin films on c-cut sapphire substrates via strain variation. *ACS Appl. Mater. Interfaces* **2017**, *9* (6), 5319−5327.

(13) Peter, A. P.; Martens, K.; Rampelberg, G.; Toeller, M.; Ablett, J. M.; Meersschaut, J.; Cuypers, D.; Franquet, A.; Detavernier, C.; Rueff, J.-P. Metal-insulator transition in ALD VO_2 ultrathin films and nanoparticles: morphological control. *Adv. Funct. Mater.* **2015**, *25* (5), 679−686.

(14) Fan, L.; Chen, Y.; Liu, Q.; Chen, S.; Zhu, L.; Meng, Q.; Wang, B.; Zhang, Q.; Ren, H.; Zou, C. Infrared response and optoelectronic memory device fabrication based on epitaxial VO_2 film. *ACS Appl. Mater. Interfaces* **2016**, *8* (48), 32971−32977.

(15) Ekstrom, E.; Hurand, S.; le Febvrier, A.; Elsukova, A.; Persson, P. O. A.; Paul, B.; Eriksson, F.; Sharma, G.; Voznyy, O.; Sangiovanni, D. G. Microstructure control and property switching in stress-free van der Waals epitaxial VO_2 films on mica. *Mater. Des.* **2023**, *229*, 111864.

(16) Ekström, E.; Hurand, S.; Yildizhan, M. M.; Elsukova, A.; Persson, P. O. Å.; Paul, B.; Ramanath, G.; le Febvrier, A.; Eriksson, F.; Eklund, P. Single-phase growth, stabilization, and electrical properties of B phase VO_2 films grown on mica by reactive magnetron sputtering. *Adv. Physics Res.* **2023**, *2* (12), 2300032.

(17) Liu, M.; Li, X.; Li, L.; Li, L.; Zhao, S.; Lu, K.; Chen, K.; Zhu, J.; Zhou, T.; Hu, C. Continuous photothermal and radiative cooling energy arvesting by VO_2 smart coatings with switchable broadband infrared emission. *ACS Nano* **2023**, *17* (10), 9501−9509.

(18) Chen, B.; Wang, X.; Li, W.; Li, C.; Wang, Z.; Guo, H.; Wu, J.; Fan, K.; Zhang, C.; He, Y.; et al. Electrically addressable integrated intelligent terahertz metasurface. *Sci. Adv.* **2022**, *8* (41), No. eadd1296.

(19) Prakash, S.; Pitchappa, P.; Agrawal, P.; Jani, H.; Zhao, Y.; Kumar, A.; Thong, J.; Linke, J.; Ariando, A.; Singh, R.; et al. Electromechanically reconfigurable terahertz stereo metasurfaces. *Adv. Mater.* **2024**, *36* (32), 2402069.

(20) Shi, R.; Chen, Y.; Cai, X.; Lian, Q.; Zhang, Z.; Shen, N.; Amini, A.; Wang, N.; Cheng, C. Phase management in single-crystalline vanadium dioxide beams. *Nat. Commun.* **2021**, *12* (1), 4214.

(21) Shi, R.; Cai, X.; Wang, W.; Wang, J.; Kong, D.; Cai, N.; Chen, P.; He, P.; Wu, Z.; Amini, A.; et al. Single-crystalline vanadium dioxide actuators. *Adv. Funct. Mater* **2019**, *29* (20), 1900527.

(22) Wang, T.; Torres, D.; Fernandez, F. E.; Green, A. J.; Wang, C.; Sepulveda, N. Increasing efficiency, speed, and responsivity of vanadium dioxide based photothermally driven actuators using single-wall carbon nanotube thin-films. *ACS Nano* **2015**, *9* (4), 4371−4378.

(23) Yuan, R.; Tiw, P. J.; Cai, L.; Yang, Z.; Liu, C.; Zhang, T.; Ge, C.; Huang, R.; Yang, Y. A neuromorphic physiological signal processing system based on VO_2 memristor for next-generation human-machine interface. *Nat. Commun.* **2023**, *14* (1), 3695.

(24) Lee, Y. J.; Kim, Y.; Gim, H.; Hong, K.; Jang, H. W. Nanoelectronics Using Metal−Insulator Transition. *Adv. Mater.* **2024**, *36* (5), No. e2305353.

(25) Feng, C.; Li, B.; Dong, Y.; Chen, X.; Zheng, Y.; Wang, Z.; Lin, H.; Jiang, W.; Zhang, S.; Zou, C.; et al. Quantum imaging of the reconfigurable VO_2 synaptic electronics for neuromorphic computing. *Sci. Adv.* **2023**, *9* (40), No. eadg9376.

(26) Chen, Y.; Fan, L.; Fang, Q.; Xu, W.; Chen, S.; Zan, G.; Ren, H.; Song, L.; Zou, C. Free-standing SWNTs/VO_2/Mica hierarchical films for high-performance thermochromic devices. *Nano Energy* **2017**, *31*, 144−151.

(27) Stinson, H. T.; Sternbach, A.; Najera, O.; Jing, R.; McLeod, A. S.; Slusar, T. V.; Mueller, A.; Anderegg, L.; Kim, H. T.; Rozenberg, M. Imaging the nanoscale phase separation in vanadium dioxide thin films at terahertz frequencies. *Nat. Commun.* **2018**, *9*, 3604.

(28) Chen, S.; Wang, Z.; Ren, H.; Chen, Y.; Yan, W.; Wang, C.; Li, B.; Jiang, J.; Zou, C. Gate-controlled VO_2 phase transition for high-performance smart windows. *Sci. Adv.* **2019**, *5* (3), No. eaav6815.

(29) Chang, T.; Cao, X.; Dedon, L. R.; Long, S.; Huang, A.; Shao, Z.; Li, N.; Luo, H.; Jin, P. Optical design and stability study for ultrahigh-performance and long-lived vanadium dioxide-based thermochromic coatings. *Nano Energy* **2018**, *44*, 256−264.

(30) Lee, D. K.; Park, Y.; Sim, H.; Park, J.; Kim, Y.; Kim, G.-Y.; Eom, C.-B.; Choi, S.-Y.; Son, J. Heterogeneous integration of single-crystalline rutile nanomembranes with steep phase transition on silicon substrates. *Nat. Commun.* **2021**, *12* (1), 5019.

(31) Jo, Y.-R.; Lee, W.-J.; Yoon, M.-H.; Kim, B.-J. In situ tracking of low-temperature VO_2 crystallization via photocombustion and characterization of phase-transition reliability on large-area flexible substrates. *Chem. Mater.* **2020**, *32* (9), 4013−4023.

(32) Gu, J.; Wei, H.; Ren, F.; Guan, H.; Liang, S.; Geng, C.; Li, L.; Zhao, J.; Dou, S.; Li, Y. VO_2 based infrared radiation regulator with excellent dynamic thermal management performance. *ACS Appl. Mater. Interfaces* **2022**, *14* (2), 2683−2690.

(33) Park, D. Y.; Joe, D. J.; Kim, D. H.; Park, H.; Han, J. H.; Jeong, C. K.; Park, H.; Park, J. G.; Joung, B.; Lee, K. J. Self-powered real-time arterial pulse monitoring using ultrathin epidermal piezoelectric sensors. *Adv. Mater.* **2017**, *29* (37), 1702308.

(34) Bakaul, S. R.; Serrao, C. R.; Lee, O.; Lu, Z.; Yadav, A.; Carraro, C.; Maboudian, R.; Ramesh, R.; Salahuddin, S. High speed epitaxial perovskite memory on flexible substrates. *Adv. Mater.* **2017**, *29* (11), 1605699.

(35) Shen, L.; Wu, L.; Sheng, Q.; Ma, C.; Zhang, Y.; Lu, L.; Ma, J.; Ma, J.; Bian, J.; Yang, Y.; et al. Epitaxial lift-off of centimeter-scaled spinel ferrite oxide thin films for flexible electronics. *Adv. Mater.* **2017**, *29* (33), 1702411.

(36) Bouaziz, J.; Cancellieri, C.; Rheingans, B.; Jeurgens, L. P. H.; La Mattina, F. Advanced epitaxial lift-off and transfer procedure for the fabrication of high-quality functional oxide membranes. *Adv. Mater. Interfaces* **2023**, *10* (2), 2201458.

(37) Bitla, Y.; Chu, Y.-H. Van der waals oxide heteroepitaxy for soft transparent electronics. *Nanoscale* **2020**, *12* (36), 18523−18544.

(38) Guo, Y.; Peng, B.; Qiu, R.; Dong, G.; Yao, Y.; Zhao, Y.; Zhou, Z.; Liu, M. Self-rolling-up enabled ultrahigh-density information storage in freestanding single-crystalline ferroic oxide films. *Adv. Funct. Mater.* **2023**, *33* (20), 2213668.

(39) Chen, B.; Zhu, W.; Wang, T.; Peng, B.; Xu, Y.; Dong, G.; Guo, Y.; Liu, H.; Huang, H.; Liu, M. Ultrahigh energy storage capacitors based on freestanding single-crystalline antiferroelectric membrane/PVDF composites. *Adv. Funct. Mater.* **2023**, *33* (36), 2302683.

(40) Cheng, Y.; Li, Y.; Dong, G.; Peng, B.; Zhou, Z.; Liu, M. Flexible multiferroic heterostructure based on freestanding single-crystalline $BaTiO_3$ membranes for spintronic devices. *Adv. Electron. Mater.* **2022**, *8* (6), 2100923.

(41) Peng, B.; Peng, R.; Zhang, Y.; Dong, G.; Zhou, Z.; Zhou, Y.; Li, T.; Liu, Z.; Luo, Z.; Wang, S.; et al. Phase transition enhanced superior elasticity in freestanding single-crystalline multiferroic $BiFeO_3$ membranes. *Sci. Adv.* **2020**, *6* (34), No. eaba5847.

(42) Liu, Y.; Cai, Y.; Zhang, Y.; Deng, X.; Zhong, N.; Xiang, P.; Duan, C. Van der waals epitaxy for high-quality flexible VO_2 film on mica substrate. *J. Appl. Phys.* **2021**, *130* (2), 025301.

(43) Ma, H.; Xiao, X.; Wang, Y.; Sun, Y.; Wang, B.; Gao, X.; Wang, E.; Jiang, K.; Liu, K.; Zhang, X. Wafer-scale freestanding vanadium dioxide film. *Sci. Adv.* **2021**, *7* (50), No. eabk3438.

(44) Li, X.; Yin, Z.; Zhang, X.; Wang, Y.; Wang, D.; Gao, M.; Meng, J.; Wu, J.; You, J. Epitaxial liftoff of wafer-scale VO_2 nanomembranes for flexible, ultrasensitive tactile sensors. *Adv. Mater. Technol.* **2019**, *4* (7), 1800695.

(45) Han, K.; Wu, L.; Cao, Y.; Wang, H.; Ye, C.; Huang, K.; Motapothula, M.; Xing, H.; Li, X.; Qi, D.-C. Enhanced metal-insulator transition in freestanding VO_2 down to 5 nm thickness. *ACS Appl. Mater. Interfaces* **2021**, *13* (14), 16688−16693.

(46) Xu, C.; Jin, C.; Chen, Z.; Lu, Q.; Cheng, Y.; Zhang, B.; Qi, F.; Chen, J.; Yin, X.; Wang, G.; et al. Transient dynamics of the phase transition in VO_2 revealed by mega-electron-volt ultrafast electron diffraction. *Nat. Commun* **2023**, *14* (1), 1265.

(47) Liu, X.; Sun, G.; Chen, P.; Liu, J.; Zhang, Z.; Li, J.; Ma, H.; Zhao, B.; Wu, R.; Dang, W. High-performance asymmetric electrodes photodiode based on Sb/WSe_2 heterostructure. *Nano Res.* **2019**, *12* (2), 339−344.

(48) Yuan, W.; Ueji, K.; Yagi, T.; Endo, T.; Lim, H. E.; Miyata, Y.; Yomogida, Y.; Yanagi, K. Control of thermal conductance across vertically stacked two-dimensional van der Waals materials via interfacial engineering. *ACS Nano* **2021**, *15* (10), 15902−15909.

(49) Deus, D. P. D. A.; Lopes, J. M. J.; Miwa, R. H. Stacking order effects on the energetics and electronic properties of n-doped graphene/h-BN van der Waals heterostructures on SiC(0001). *Carbon* **2023**, *213*, 118244.

(50) Jin, G.; Lee, C.-S.; Okello, O. F. N.; Lee, S.-H.; Park, M. Y.; Cha, S.; Seo, S.-Y.; Moon, G.; Min, S. Y.; Yang, D.-H. Heteroepitaxial van der Waals semiconductor superlattices. *Nat. Nanotechnol.* **2021**, *16* (10), 1092.

(51) Li, Y.; Ma, H.; Tang, F.; Li, C.; Wang, B.; Song, X.; Liu, K.; Zhang, X. Direct laser writing of multishaped VO_2 microactuators based on freestanding VO_2 film. *Adv. Mater. Technol.* **2023**, *8* (1), 2200977.

(52) Chae, J.-Y.; Lee, D.; Lee, D. W.; Woo, H.-Y.; Kim, J. B.; Paik, T. Direct transfer of thermochromic tungsten-doped vanadium dioxide thin-films onto flexible polymeric substrates. *Appl. Surf. Sci.* **2021**, *545*, 148937.

(53) Shen, N.; Chen, S.; Shi, R.; Niu, S.; Amini, A.; Cheng, C. Phase transition hysteresis of tungsten doped VO_2 synergistically boosts the function of smart windows in ambient conditions. *ACS Appl. Electron. Mater.* **2021**, *3* (8), 3648−3656.

(54) Zhao, Z.; Li, J.; Ling, C.; Zhao, X.; Zhao, Y.; Jin, H. Electric field driven abnormal increase in conductivity of tungsten-doped VO_2 nanofilms. *Thin Solid Films* **2021**, *725*, 138643.

(55) Tang, C.; Georgopoulos, P.; Fine, M. E.; Cohen, J. B.; Nygren, M.; Knapp, G. S.; Aldred, A. Local atomic and electronic arrangements in $W_XV_{1-X}O_2$. *Phys. Rev. B* **1985**, *31* (2), 1000−1011.

(56) Liu, D.; Zhang, Q.; Chen, X.; Dai, H.; Zhai, X.; Gong, G.; Shang, C.; Xie, L.; Wang, X. Defect engineering of vanadium dioxide by W ion doping with enhanced electrochemical performance. *Ceram. Int.* **2023**, *49* (14), 23704−23713.

(57) Chen, B.; Wu, J.; Li, W.; Zhang, C.; Fan, K.; Xue, Q.; Chi, Y.; Wen, Q.; Jin, B.; Chen, J.; et al. Programmable terahertz metamaterials with non-volatile memory. *Laser Photonics Rev.* **2022**, *16* (4), 2100472.

(58) Xiao, L.; Ma, H.; Liu, J.; Zhao, W.; Jia, Y.; Zhao, Q.; Liu, K.; Wu, Y.; Wei, Y.; Fan, S. Fast adaptive thermal camouflage based on flexible VO_2/graphene/CNT thin films. *Nano Lett.* **2015**, *15* (12), 8365−8370.

(59) Li, Y.; Ma, H.; Wang, Y.; Ding, J.; Qi, L.; Fu, Y.; Ning, R.; Rong, L.; Wang, D.; Zhang, X. Electrically driven active VO_2/MXene metasurface for the terahertz modulation. *Appl. Phys. Lett.* **2022**, *121* (24), 241902.

(60) Lee, S.; Cheng, C.; Guo, H.; Hippalgaonkar, K.; Wang, K.; Suh, J.; Liu, K.; Wu, J. Axially engineered metal-insulator phase transition by graded doping VO_2 nanowires. *J. Am. Chem. Soc.* **2013**, *135* (12), 4850−4855.

(61) Zhu, H.; Li, Q.; Tao, C.; Hong, Y.; Xu, Z.; Shen, W.; Kaur, S.; Ghosh, P.; Qiu, M. Multispectral camouflage for infrared, visible, lasers and microwave with radiative cooling. *Nat. Commun.* **2021**, *12* (1), 1805.

(62) Wei, H.; Gu, J.; Ren, F.; Geng, C.; Guan, H.; Liang, S.; Fan, Q.; Zhao, J.; Wang, C.; Dou, S.; et al. Kirigami-inspired reconfigurable thermal mimetic device. *Laser Photon. Rev.* **2022**, *16* (12), 2200383.

(63) Mogunov, I. A.; Lysenko, S.; Fedianin, A. E.; Fernandez, F. E.; Rua, A.; Kent, A. J.; Akimov, A. V.; Kalashnikova, A. M. Large non-thermal contribution to picosecond strain pulse generation using the photo-induced phase transition in VO_2. *Nat. Commun.* **2020**, *11* (1), 1690.

(64) Fan, X.; Hehn, M.; Wei, G.; Malinowski, G.; Huang, T.; Xu, Y.; Zhang, B.; Zhang, W.; Lin, X.; Zhao, W. On/off ultra-short spin current for single pulse magnetization reversal in a magnetic memory using VO_2 phase transition. *Adv. Electron. Mater.* **2022**, *8* (10), 2200114.

(65) Wang, T.; Torres, D.; Fernandez, F. E.; Wang, C.; Sepulveda, N. Maximizing the performance of photothermal actuators by combining smart materials with supplementary advantages. *Sci. Adv.* **2017**, *3* (4), 1602697.